applied sciences

MDPI

Article

Co-Design of Mechanical and Vibration Properties of a Star Polygon-Coupled Honeycomb Metamaterial

Jiawang Yong [1], Wanting Li [1], Xiaojun Hu [2,*], Zhishuai Wan [3], Yiyao Dong [1] and Nenglian Feng [1]

[1] Department of Traffic Engineering, Beijing University of Technology, Beijing 100124, China; yongjw@bjut.edu.cn (J.Y.); liwting@emails.bjut.edu.cn (W.L.); dongyiyao@emails.bjut.edu.cn (Y.D.); fengnl@bjut.edu.cn (N.F.)
[2] School of Mechanical, Electronic and Control Engineering, Beijing Jiaotong University, Beijing 100044, China
[3] Beijing Key Laboratory of Lightweight Multi-Functional Composite Materials and Structures, Institute of Advanced Structure Technology, Beijing Institute of Technology, Beijing 100081, China; wanzhishuai@bit.edu.cn
* Correspondence: xjhu@bjtu.edu.cn

Abstract: Based on the concept of component assembly, a novel star polygon-coupled honeycomb metamaterial, which achieves a collaborative improvement in load-bearing capacity and vibration suppression performance, is proposed based on a common polygonal structure. The compression simulation and experiment results show that the load-bearing capacity of the proposed metamaterial is three times more than that of the initial metamaterial. Additionally, metal pins are attached and particle damping is applied to the metamaterial to regulate its bandgap properties; the influence of configuration parameters, including the size, number, position, and material of the metal pins, on bandgaps is also investigated. The results show that the bandgap of the proposed metamaterial can be conveniently and effectively regulated by adjusting the parameters and can effectively suppress vibrations in the corresponding frequency band. Particle damping can be used to continuously adjust the frequency of the bandgap and further enhance the vibration suppression capacity of the metamaterial in other frequency bands. This paper provides a reference for the design and optimization of metamaterials.

Keywords: star polygon-coupled honeycomb metamaterial; mechanical properties; vibration suppression; bandgap; load-bearing capacity

check for updates

Citation: Yong, J.; Li, W.; Hu, X.; Wan, Z.; Dong, Y.; Feng, N. Co-Design of Mechanical and Vibration Properties of a Star Polygon-Coupled Honeycomb Metamaterial. *Appl. Sci.* **2024**, *14*, 1028. https://doi.org/10.3390/app14031028

Academic Editor: Roberto Zivieri

Received: 19 December 2023
Revised: 20 January 2024
Accepted: 21 January 2024
Published: 25 January 2024

Copyright: © 2024 by the authors. Licensee MDPI, Basel, Switzerland. This article is an open access article distributed under the terms and conditions of the Creative Commons Attribution (CC BY) license (https://creativecommons.org/licenses/by/4.0/).

1. Introduction

Metamaterials are artificial composite materials with a periodic arrangement of elements and remarkable physical properties that do not exist in natural materials. Well-designed metamaterials exhibit excellent properties in many fields, such as mechanics [1–4], acoustics [5–9], optics [10–13], and electromagnetics [14–16]. Due to these special properties, metamaterials have been widely used in transportation [17,18], the automobile industry [19,20], aerospace [21,22], and other fields.

Artificially designed and manufactured metamaterials have significant advantages in regulating and optimizing various properties. Zhang et al. [23] obtained an ultra-wide low-frequency bandgap in acoustic metamaterials through an optimized system topology method. By investigating the bandgap characteristics of acoustic metamaterials, Liu et al. [24] demonstrated the superiority of the bandgaps generated by the proposed configuration, and realized ultra-low-frequency vibration control. Wang et al. [25] improved a bifocal piezoelectric metamaterial beam, and the co-operative effect of vibration isolation and energy harvesting was verified through simulations. In addition to acoustics and optics, metamaterials also have extensive applications in impact resistance. Ye et al. [26] proposed a full-cycle interactive and progressive method to determine the energy absorption characteristics of metamaterials and verified that hand-shaped metamaterials have

good energy absorption and impact resistance performance. Chen et al. [27] presented a reusable composite mechanical metamaterial and verified its properties via experiments and simulations. It was found that the proposed metamaterial has an acceptable impact resistance performance and no plastic deformation occurs. Alomarah et al. [28] developed a butterfly-shaped auxetic metamaterial and investigated its mechanical properties and energy absorption effects. The results show that the metamaterial has excellent and controllable mechanical properties and its specific energy absorption rate is higher than that of re-entrant and hand-shaped honeycomb metamaterials. These studies improved the performance of metamaterials by modifying algorithms and configurations, showing the great advantages of metamaterials in performance design.

The mechanical properties of metamaterials, including their deformation characteristics, load-bearing capacity, and vibration suppression capability, are important in engineering applications. Li et al. [1] designed a novel auxetic metamaterial, investigated its deformation mechanism through experiments, and comprehensively examined the influence of geometric features on its mechanical properties. Zhang et al. [29] designed a mechanical metamaterial that exhibits regular local deformation under static load and provided valuable insights into the local deformation and phase transition phenomena of these kinds of metamaterials. Dong et al. [30] developed a novel auxetic metamaterial and evaluated its auxetic properties under quasi-static compression; the study confirmed that the proposed configuration has good subsidiarity and stiffness. Zhang et al. [31] designed a reconfigurable metamaterial based on an ordinary steady-state metamaterial, and verified experimentally that the bearing capacity of the optimized metamaterial is four times more than that of the switching force. Zhang et al. [32] designed a novel material by adding parts to the traditional returnable configuration, and the self-adjusting stiffness properties and stability improvement of the proposed metamaterial were demonstrated through simulations. These studies modified the structures of conventional metamaterials and evaluated the advantages of configuration modification by combining experimental and simulation results, thereby providing a reference for this work.

The bandgap caused by the periodic structure is a special vibration suppression characteristic of metamaterials; it has always been the focus of engineering applications using these materials. He et al. [33] combined bandgaps and the frequency domain to analyze the vibration suppression performance of a local resonant metamaterial, providing a theoretical foundation for related research. An interconnected metamaterial was proposed by Jin et al. [34]; it simplified the fabrication and installation processes, and the vibration isolation capacity of the material was validated by extracting the Bloch mode according to the modal strain energy. Bai et al. [35] designed an aseismatic metamaterial and investigated its bandgap characteristics via the transfer matrix method; the results show that the acceleration amplitude decreases during wave propagation, which demonstrates the material's vibration suppression performance. Although there are many methods through which to improve vibration suppression performance, bandgap-induced vibration suppression is regarded as one of the most special and effective methods for metamaterials. Vibrations cannot pass through the bandgap frequency range in the form of elastic waves, but the frequency of the vibration source may change in engineering applications. Therefore, the adjustment method for bandgaps is also a focus for the vibration design of metamaterials. Das et al. [36] studied the bandgap characteristics of cells with different shapes through a combination of experiments and simulations and confirmed that cell shape can affect the bandgap. Liu et al. [24] presented an I-shaped radial elastic metamaterial and found that the material can generate ultra-low-frequency wide bandgaps under quasi-static conditions. Moreover, Bae [37], Yang [38], Bera [39], and Muhammad [40] et al. have investigated the influence of geometric and material parameters on bandgap properties. Gerard [41], Zhao [42], and De Ponti [43] proposed 3D metamaterial structures and proved that three-dimensional structures can also be adjusted to generate ideal bandgaps, and their findings are helpful when considering the vibration suppression of metamaterials in low-frequency bands.

The abovementioned works have made many achievements in independently improving load-bearing capacity and vibration suppression performance. However, achieving both good load-bearing capacity and vibration resistance in a metamaterial remains a considerable challenge. In this paper, based on a polygon metamaterial, a novel star polygon-coupled honeycomb metamaterial is proposed, which generates low-frequency bandgaps and achieves a great improvement in load-bearing capacity in contrast with the initial metamaterial. Meanwhile, the influence of configuration parameters (including the size, number, position, and material of the metal pins) on the load-bearing capacity and bandgap properties is investigated. Additionally, particle damping is introduced into the metamaterial to continuously adjust the bandgap frequency and improve vibration attenuation in frequency ranges without bandgaps. The simulation and experimental results demonstrate that the proposed metamaterial achieves a collaborative improvement of bearing capacity and vibration suppression performance.

The rest of the paper is structured as follows. In Section 2, the structure and geometric parameters of the unit cells are explained. In Section 3, the stress–strain characteristics and load-bearing properties of the metamaterials are studied. The bandgap properties of the metamaterials and the influence of configuration parameters on bandgap properties are studied in Section 4. In Section 5, the vibration suppression performance of the metamaterials is evaluated by simulations and experiments. The findings of this work are summarized in Section 6.

2. Structure Design of the Star Polygon-Coupled Honeycomb Metamaterial

Shown in Figure 1 are the structural features of the proposed novel star polygon-coupled honeycomb metamaterial (SPCHM). For generating more local resonance bandgaps, the SPCHM is created by coupling a cross-linked star-shaped structure into the horizontal connecting rod of the initial metamaterials (IM), as shown in Figure 1b. Furthermore, the connecting nodes are designed as circular rings, which can improve the designability on the load-bearing and vibration suppression capabilities. The definition and value of the geometric parameters are reflected in Figure 1d and Table 1, respectively. a_x and a_y stand for the length and width of the unit cell, accordingly. d denotes the rod width, θ represents the angle between two adjacent rods, and r_1 and r_2 are the inner and outer radius of the rings, respectively. The width of the rods is 1.2 mm.

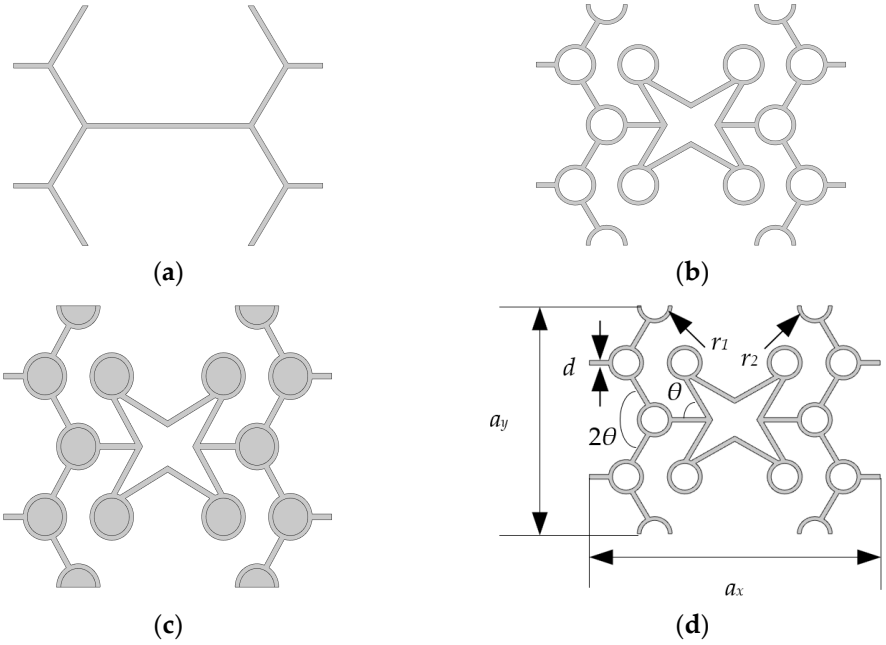


Figure 1. Schematic diagram of (**a**) IM, (**b**) SPCHM, (**c**) SPCHM with pins, and (**d**) geometric dimensions of the SPCHM.

Table 1. Parameter values of the unit cell.

a_x (mm)	a_y (mm)	d (mm)	θ (°)	r_1 (mm)	r_2 (mm)
75	60	1.2	60	4	5

3. Stress–Strain Characteristics of the Metamaterials by Simulation and Experiment

Three-dimensional printing, which is also known as additive manufacturing, is a rapid prototyping technology to construct 3D objects through the method of layer-by-layer printing. The stereolithography (SLA) 3D printing technology, which is one of the most widely used rapid prototyping technologies to cure layers of resin and create 3D objects using ultraviolet light, was adopted to manufacture the proposed metamaterials. The metamaterials used in the experiments were manufactured by the company named WENEXT in Shenzhen, China, and an industrial SLA 3D printer Lite600HD (UnionTech, Shanghai, China) was employed. The layer thickness precision of the Lite600HD is up to 0.05 mm and the printing speed is 7 mm/s. The resin material WEILAI8000 (WL8000), which is produced by the Royal DSM Group of the Netherlands with excellent properties, smooth surface, high precision, and water and moisture resistance, was used.

The build orientation affects the strength, accuracy, and surface finish of the 3D printing parts. When the tension forces are perpendicular to the printing layers, part weakness tends to occur. In contrast, the printed parts are stronger if the tension forces are parallel. Therefore, the proposed metamaterials were printed in an orientation so that layers aligned with the axis where tension forces were highest or in an orientation so that layers intersected the axis where compression forces were highest. In order to achieve excellent characteristics while ensuring the printing accuracy, the thicknesses of the rods and rings of the proposed metamaterials were designed to be 1.2 mm and 1 mm, respectively. The dimensional accuracy of the 3D-printed samples is 0.05 mm and the relative density errors are below 2%, which ensures that the samples meet the requirements and can be used for experiments. The WL8000-based structures are fastened to the upper and lower aluminum strips and the assembly pins are made of copper, as shown in Figure 2a–c. The properties of the materials are listed in Table 2. Furthermore, numerical simulations and actual experiments were carried out to investigate the stress–strain characteristics of the involved structures.

Table 2. Properties of the materials.

Material	Density (kg/m³)	Elastic Modulus (GPa)
WL8000	1120	2.65
Aluminum	2700	71
Copper	8960	117
Tungsten	19,350	411

Firstly, a two-dimensional cell was built in Abaqus CAE 2018 (Dassault aircraft company, Paris, France), as shown in Figure 1, and then the required number of cells was extended in the horizontal and vertical directions. A total of five cells in the horizontal direction and eight cells in the vertical direction were set to generate the proposed structure in this paper. With the aluminum strips and metal pins assembled in the desired positions, the entire model is combined into a whole structure, as shown in Figure 2a–c. The thickness of the model was set to 20 mm, which is equal to that of the experimental samples. The specific material properties are shown in Table 2. To ensure that there were at least 10 elements in the shortest wavelength to guarantee accuracy, the maximum mesh size was set to 0.3 mm. In addition, the bottom surface of the upper aluminum strip and the two sides of the lower aluminum strip were set to be completely fixed. The load force F was applied to the midpoint of the upper surface of the aluminum strip and the maximum deformation displacement was set to 15 mm, starting at 0 mm and gradually increasing to 15 mm.

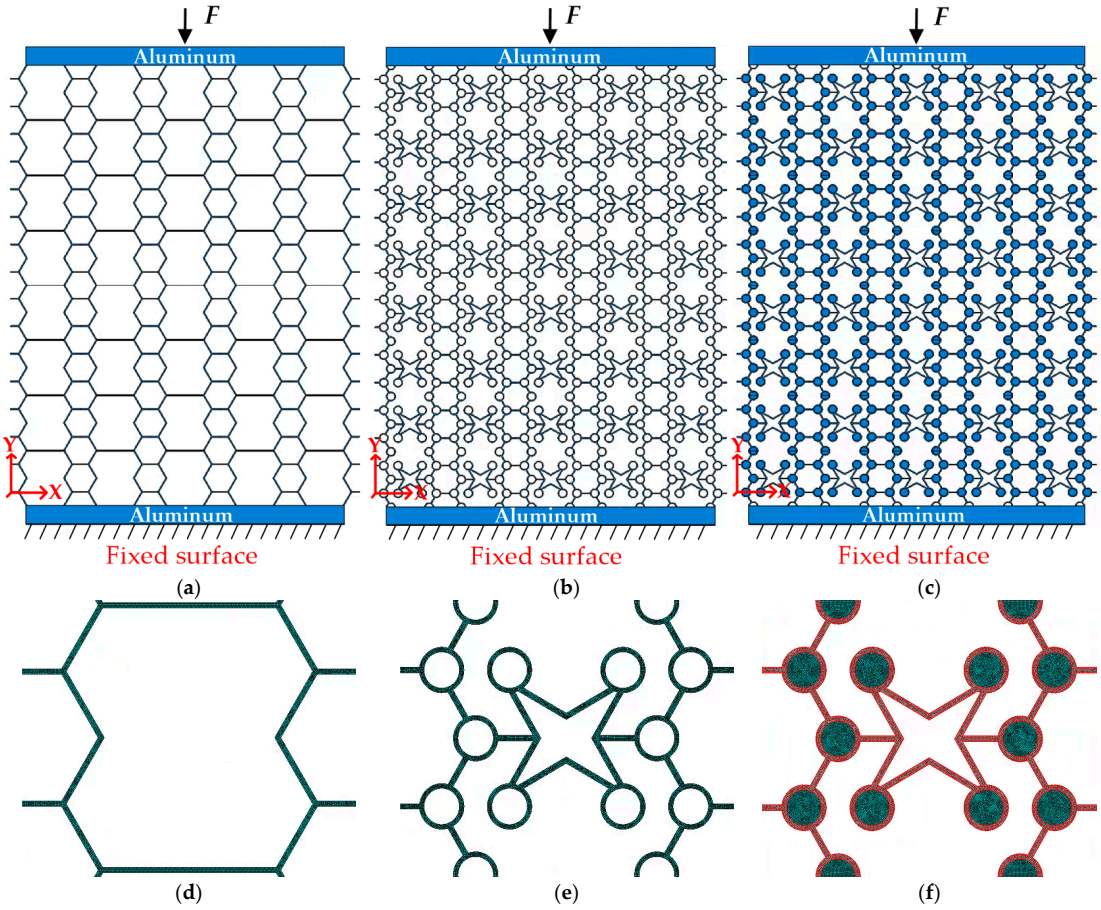


Figure 2. Simulation structures and finite element meshes. (**a**) Simulation structure of the IM; (**b**) simulation structure of the SPCHM; (**c**) simulation structure of the SPCHM with copper pins; (**d**) finite element mesh of the IM; (**e**) finite element mesh of the SPCHM; (**f**) finite element mesh of the SPCHM with copper pins.

Static compression experiments were conducted using the Instron Legend 2367 universal testing machine (UTM) (INSTRON Corporation, Boston, MA, USA), and Figure 3a illustrates the main components of the UTM. The load conditions of the experiments were the same as with the simulations, and the compression displacement was controlled from 0 to 15 mm with a velocity of 0.01 mm/s. However, some of the structures failed before reaching the final displacement, and this problem comes down to the material properties of the WL8000. The testing was stopped when the sample was damaged.

Figure 3b–d show the compression histories of the IM, SPCHM, and SPCHM with copper pins generated from the simulations and experiments, respectively, and the small figures A–C are the shapes of the structures by simulation and experiment under different load conditions. As can be seen from the figure, the maximum errors of the three metamaterials between simulation and experiment occur at the end of the experiments. There is little difference in the overall stiffness value of the sample during elastic deformation in the simulation and experiment, and the root mean square errors of the three metamaterials are 5.7%, 6.5%, and 9.88%, respectively. The reason for the error is that, with the increase in the deformation load, the sample is slightly bent along the thickness direction in the experiment but it does not happen in the simulation, so this leads to the experimental value being slightly smaller than that of the simulation. In addition, the manufacture error of the sample is also one source of the testing error. From Figure 3b,c, the pressures to cause 1% deformation of the IM and SPCHM are about 16 kPa and 68 kPa, accordingly, and the mass of the IM and SPCHM are 0.96 kg and 1.26 kg, respectively. The stiffness of the SPCHM is improved by 325% compared to that of the IM, while the mass of the SPCHM is only 23.8%

heavier than that of the IM, which indicates that the SPCHM shows an improvement in stiffness owing to the addition of rings. Therefore, the stable load-bearing capacity of the SPCHM increases with the improvement in stiffness. As drawn in Figure 3d, the pressure of the SPCHM with copper pins is up to about 110 kPa at the 1% deformation point and the mass of the SPCHM with copper pins is 5.49 kg. The stiffness of the SPCHM with copper pins is 62% higher than that of the SPCHM, and the mass of the SPCHM with copper pins is 335% heavier than that of the SPCHM. Although the SPCHM with copper pins provides the potential for heavier load-bearing applications, it requires a significant increase in mass.

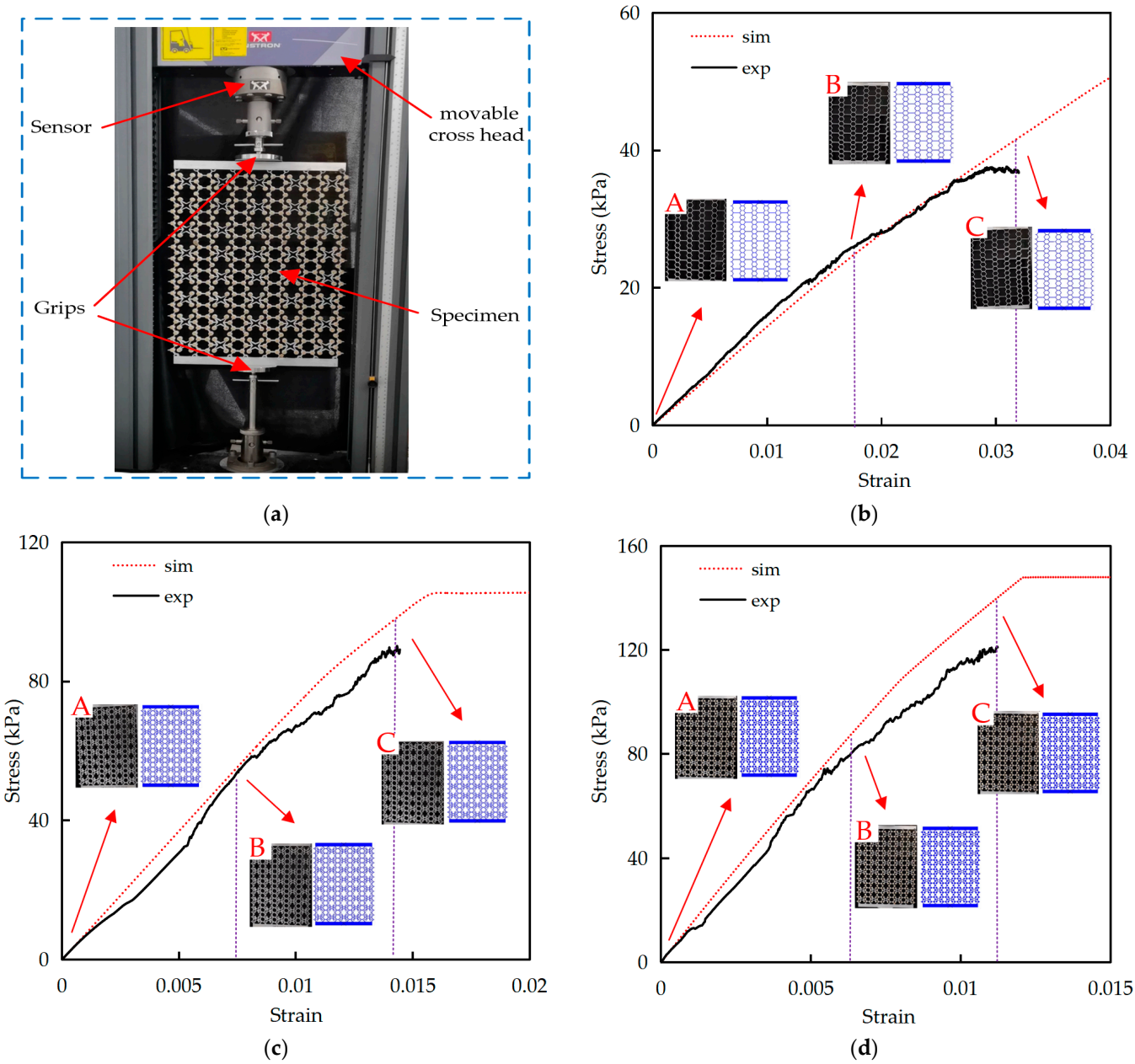


Figure 3. Stress–strain characteristics of the metamaterials by simulation and experiment: (**a**) experimental equipment; (**b**) IM; (**c**) SPCHM; (**d**) SPCHM with copper pins.

4. Comparison and Analysis of the Bandgap Properties

In the engineering applications which are sensitive to vibration, such as aviation, aerospace, navigation, and vehicles, the vibration isolation performance will significantly affect the safety and reliability of the system, and one of the biggest challenges of vibration

isolation structures is to achieve wide and low-frequency bandgaps. Therefore, this section concentrates on the bandgap performances of the IM and SPCHM and further comparing the bandgaps of the SPCHMs with different structural parameters and, finally, establishes a design method of the bandgap.

4.1. Calculation of Bandgap Properties

It is assumed that the damping and body forces are not considered; the propagation of elastic waves in two-dimensional structures can be expressed by Equation (1) according to the elastic dynamics [44].

$$\rho(\mathbf{p})\ddot{\mathbf{L}}(\mathbf{p}) = \nabla[\lambda(\mathbf{p}) + 2\mu(\mathbf{p})][\nabla\mathbf{L}(\mathbf{p})] - \nabla \times [\mu(\mathbf{p})\nabla \times \mathbf{L}(\mathbf{p})] \quad (1)$$

where ρ represents the mass density, $\mathbf{L}$ is the displacement vector, $\mathbf{p} = (x, y)$ denotes the position vector, and ∇ indicates the differential operator. λ and μ are constants and can be used to express Young's modulus E and Poisson's ratio v as:

$$E = \frac{\mu(3\lambda + 2\mu)}{\lambda + \mu}, v = \frac{\lambda}{2(\lambda + \mu)} \quad (2)$$

$\mathbf{L}$ can be further extended in accordance with the Bloch's theorem as:

$$\mathbf{L}(\mathbf{p}, \mathbf{k}) = \mathbf{L}(\mathbf{p})e^{\delta(\omega \mathrm{t} - \mathbf{pk})} \quad (3)$$

in which ω and t represent the angular frequency and time, accordingly. $\mathbf{k}$ denotes the wave vector of the lattice, $\delta = \sqrt{-1}$.

Since the proposed structures are periodic, $\mathbf{L}$ is a periodic function that has the same periodicity with the proposed structures, and the following relationship is possessed:

$$\mathbf{L}(\mathbf{p}, \mathbf{k}) = \mathbf{L}(\mathbf{p}, \mathbf{k} + \mathbf{R}) \quad (4)$$

where $\mathbf{R}$ stands for the lattice vector. Combining Equations (3) and (4), we have:

$$\mathbf{L}(\mathbf{p} + \mathbf{R}, \mathbf{k}) = \mathbf{L}(\mathbf{p})e^{\delta(\omega \mathrm{t} - \mathbf{pk})} \quad (5)$$

Substituting Equation (5) into Equation (1), after some manipulations, the following eigenvalue equation is derived:

$$\left(\mathbf{K} - \omega^2\mathbf{M}\right)\mathbf{Y} = 0 \quad (6)$$

in which $\mathbf{K}$ stands for the stiffness matrix, $\mathbf{M}$ denotes the mass matrix, and $\mathbf{Y}$ is the displacement vector of the nodes.

4.2. Comparison of Bandgap Properties between the IM and SPCHM

The bandgaps of different metamaterials were simulated by the multi-physics software COMSOL Multiphysics 6.0 (COMSOL Inc., Stockholm, Sweden). The mesh size has a great influence on the calculation accuracy, and the maximum mesh is set to 0.3 mm. The finite element meshes are shown in Figure 4e–g.

The cells of the IM, SPCHM, and SPCHM with metal pins during simulation and experiment are shown in Figure 4a–c, respectively. Figure 4d represents the Brillouin zone of the periodic lattice, along with four marked intersection points named O, 1, 2, and 3, accordingly. The software performs frequency scanning in the order of O-1-2-3-O and, finally, obtains the bandgap properties of the scanned metamaterials.

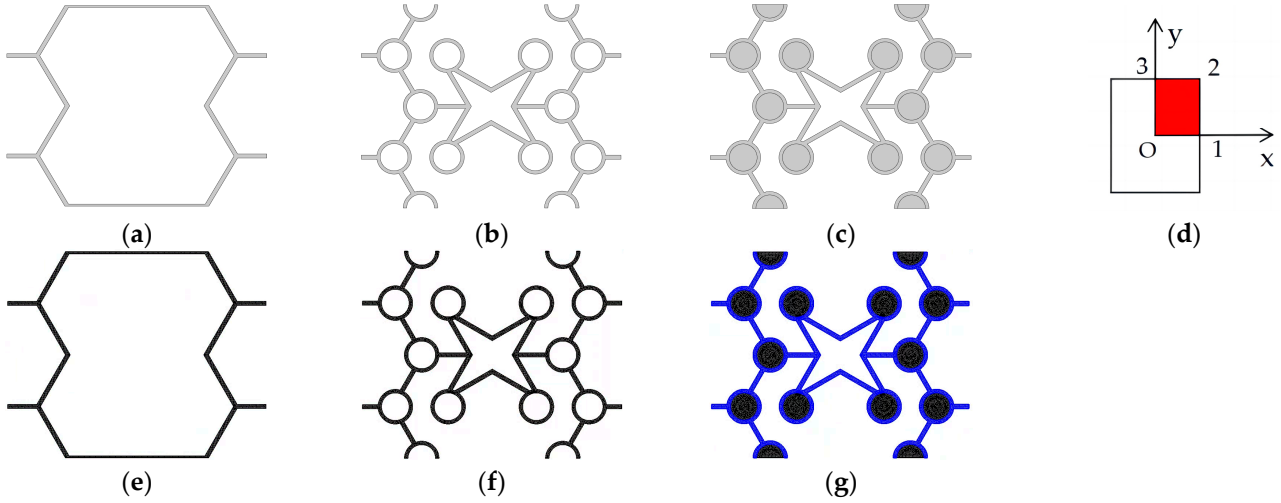


Figure 4. Diagrams for bandgap simulation: (**a**) unit cell of the IM; (**b**) unit cell of the SPCHM; (**c**) unit cell of the SPCHM with pins; (**d**) Brillouin zone of periodic lattices, (**e**) finite element mesh of the IM; (**f**) finite element mesh of the SPCHM; (**g**) finite element mesh of the SPCHM with copper pins.

The first 30 dispersion curves of the IM, SPCHM, and SPCHM with copper pins are drawn in Figure 5; the bandgaps are highlighted by red, the letters A-J represent the frequency ranges of different bandgaps, and the number 1 and 2 indicate the highest and lowest frequencies of corresponding bandgap, respectively. Figure 6 indicates the vibration mode shapes of the specific points marked in Figure 5. From the first 30 dispersion curves of the IM, the frequency band of the first bandgap (A2–A1) is from 1600 Hz to 2500 Hz. As shown in Figure 6, these kinds of mode shapes (A–E) have an overwhelming negative effect on the adjustment of the bandgaps, especially for the low-frequency bandgaps. However, changing the nodes to circular rings can change the overall mass, and the addition of the pins further increases the mass of the nodes, which changes the mass distribution and stiffness of the SPCHM-based structure, thus making its modal mode different from that of the IM and thereby changing the frequency of the bandgap. Based on Equation (6), the introduction of rings and metal pins can increase the local stiffness of the unit cell, making it possible to obtain low-frequency local resonant mode. Therefore, it is possible to create a bandgap by adjusting the design parameters.

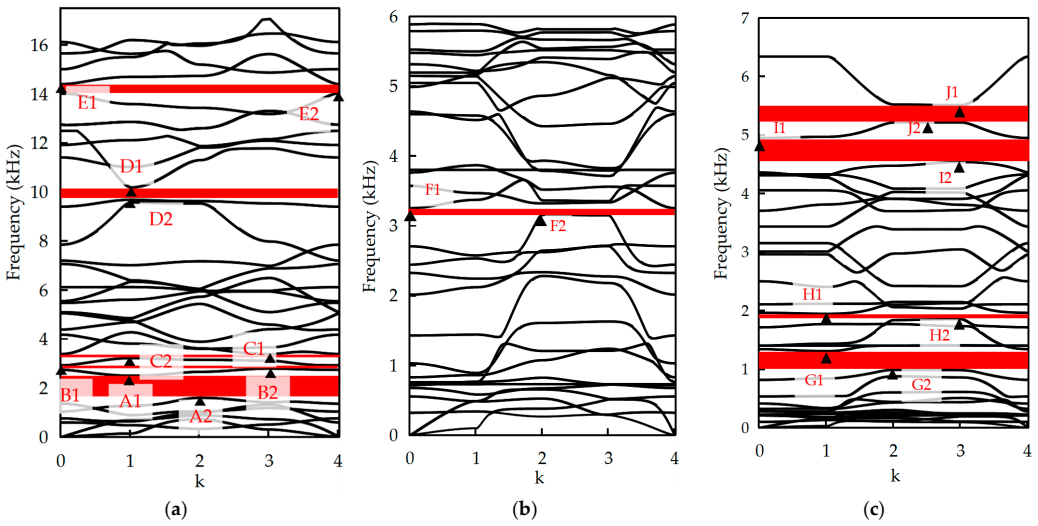


Figure 5. Dispersion curves of the metamaterials: (**a**) IM; (**b**) SPCHM; (**c**) SPCHM with copper pins. the letters A–J represent the frequency ranges of different bandgaps, and the number 1 and 2 indicate the highest and lowest frequencies of corresponding bandgap, respec-tively.

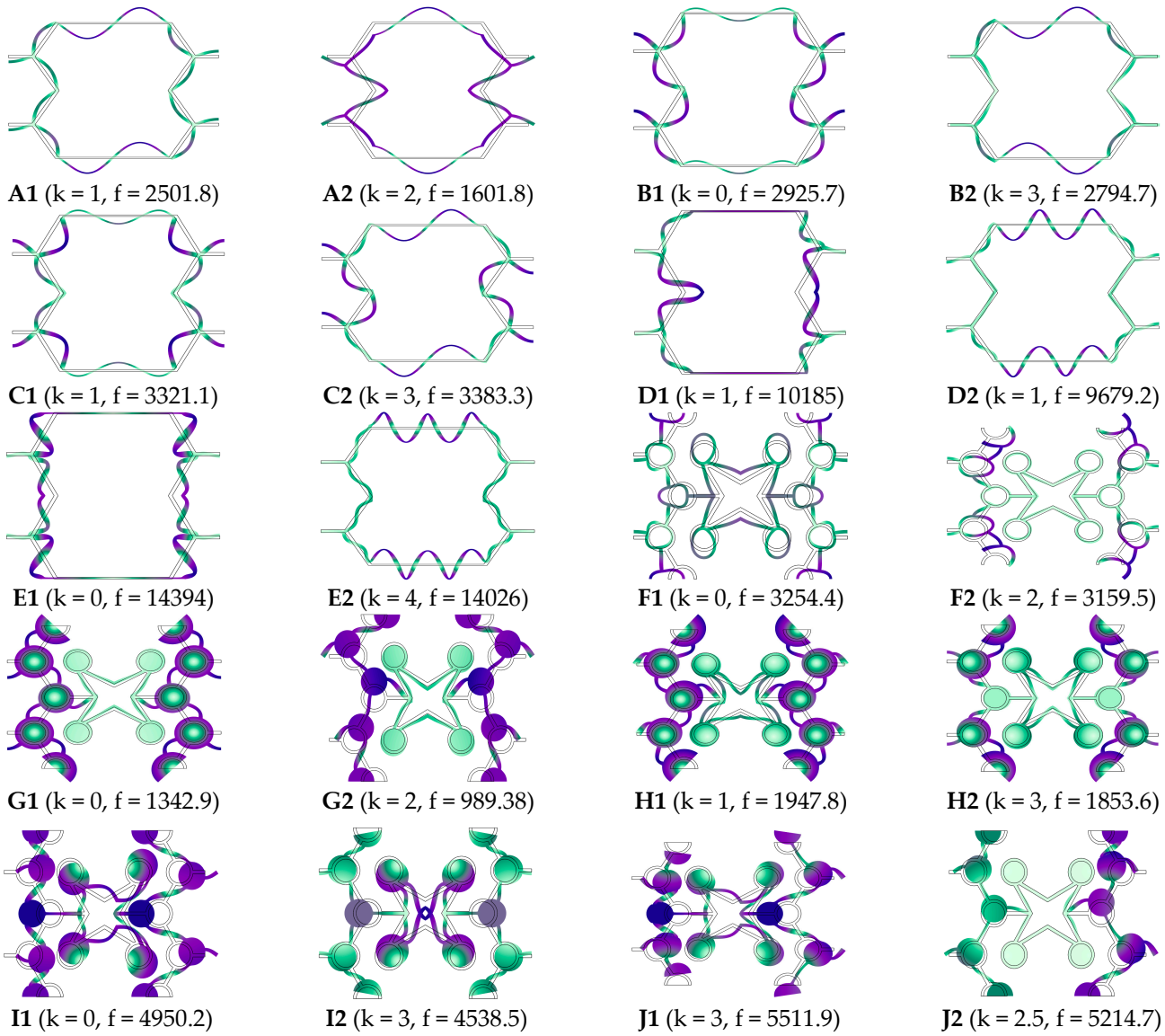


Figure 6. Vibration shapes corresponding to specific points.

The frequency of the first 30 dispersion curves of the SPCHM, which varies from 0 to about 6 kHz, is much lower than that of the IM. And the first bandgap of the SPCHM has higher frequency and narrower bandwidth compared to the IM, as marked by the red region from 3159 Hz to 3254 Hz. However, according to the modes of points F1 and F2 shown in Figure 6, the introduction of rings improves the local stiffness of the cell and results in more deformation forms between rods and rings, which makes the bandgap change internally and it indicates that the bandgap properties of the SPCHM can be regulated by changing the size of the rings or adding pins of different materials into the rings. Therefore, the factors, which could significantly influence the mode deformation of the unit cell, should be considered for generating specific bandgaps.

The mass distribution of the cell changes dramatically when the metal pins are inserted into the rings. The change in mass generates new local resonant modes, which have better energy absorption capacity, and the width and frequency of the bandgaps are changed. As can be seen from Figure 5c, four more bandgaps are generated after the addition of copper pins, and the frequency ranges are from 989 Hz to 1343 Hz, 1853 Hz to 1947 Hz, 4538 Hz to 4950 Hz, and 5214 Hz to 5512 Hz, respectively. Thus, the insertion of metal pins not only decreases the starting frequency of the first bandgap but also increases the number of

bandgaps. Combining with Figure 5b, it can be seen that the frequency of the first bandgap formed after the addition of metal pins decreases significantly from 3150 Hz to 980 Hz.

By comparing the dispersion curves of Figure 5a,b and combining with the above analysis, it can be seen that the stiffness of the IM is lower and its first bandgap is located at a lower frequency. According to the modal deformations at points A1, B2, D2, and E2 in Figure 6, the vibration shapes reveal that the horizontal long rod is a key component affecting the frequencies of the local modes, and a star shape is added in the middle of the long rod to adjust the bandgap properties. The introduction of the star and ring configurations increase the stiffness of the metamaterial. However, the first bandgap has a greatly higher frequency and narrower bandwidth than that of the IM. And, based on Equation (6), when the stiffness is enhanced, for generating lower frequency modes, the mass of the local structure should be increased. Thus, the introduction of metal pins is naturally considered for obtaining more local resonant modes, which may generate more local resonance bandgaps. Figure 5 shows that the introduction of metal pins generates better bandgaps and increases the stiffness of the metamaterials. Figure 6G–J show the mode deformations of the cell at different frequencies, which determine the bandgaps of the metamaterial. The results indicate that the size and distribution of pins can impact the local resonant modes, which has the potentiality for generating better bandgaps.

The aforementioned analysis suggests that the mode shapes have a significant impact on bandgap properties and the configuration parameters affect the mode shapes significantly. Thus, it is worthwhile to figure out the influence of the configuration parameters on bandgap.

4.3. Effects of the Configuration Parameters

4.3.1. Materials of the Inserted Pins

Drawn in Figure 7 are the bandgap properties of the SPCHM with different materials of pins, including aluminum, copper, and tungsten; the first bandgaps are marked in red and the rest in orange. It can be clearly seen that the addition of pins has an effect on the vibration mode of the proposed metamaterial and, thereby, changes the bandgap distribution. Comparing with Figure 4b, the insertion of metal pins significantly increases the mass at the nodes; since the Young's modulus of metal is much higher than that of the WL8000, the pins could be equivalent to rigid bodies in contrast with the external plastic material. Therefore, the interaction between the two materials changes the modes of points F1 and F2, causing the variation in bandgaps. For the first 30 dispersion curves of the three kinds of pins, the frequencies vary from 0 to 9100 Hz, 6300 Hz, and 4400 Hz, respectively. From aluminum to copper and then to tungsten, the mass of pin increases as density gradually raises and the dispersion curves move downward from the aluminum pins more than 9000 Hz to the tungsten pins less than 4500 Hz. Furthermore, all the frequencies of the four bandgaps decrease with the increase in pin mass.

With regard to the first bandgaps generated by the SPCHM with different pins, the frequency ranges are from 1640 Hz to 1880 Hz, 1000 Hz to 1300 Hz, and 680 Hz to 980 Hz, respectively. The frequency range of the first bandgap, where the vibration is attenuated dramatically, decreases strongly from the SPCHM with aluminum pins to that of tungsten pins. On the other hand, there are some differences between the widths of the first bandgap of the three structures, and, to be precise, the width values of the three candidates are 240 Hz, 300 Hz, and 300Hz, accordingly. Although the width of the first bandgap of the SPCHM with copper pins has been slightly broadened compared with that of the SPCHM with aluminum pins, the width of the SPCHM with tungsten pins does not continue to increase. As a consequence, for the same size of pins, the width of the first bandgap rises with the increase in pin mass until the mass reaches a certain threshold, where the width will basically remain unchanged.

The adoption of pins of different materials can effectively control the frequency and width of the bandgap, which offers the potential to adjust and optimize the bandgaps.

This approach can also be applied for vibration control and energy absorption, which requires a more precise control of the bandgap properties.

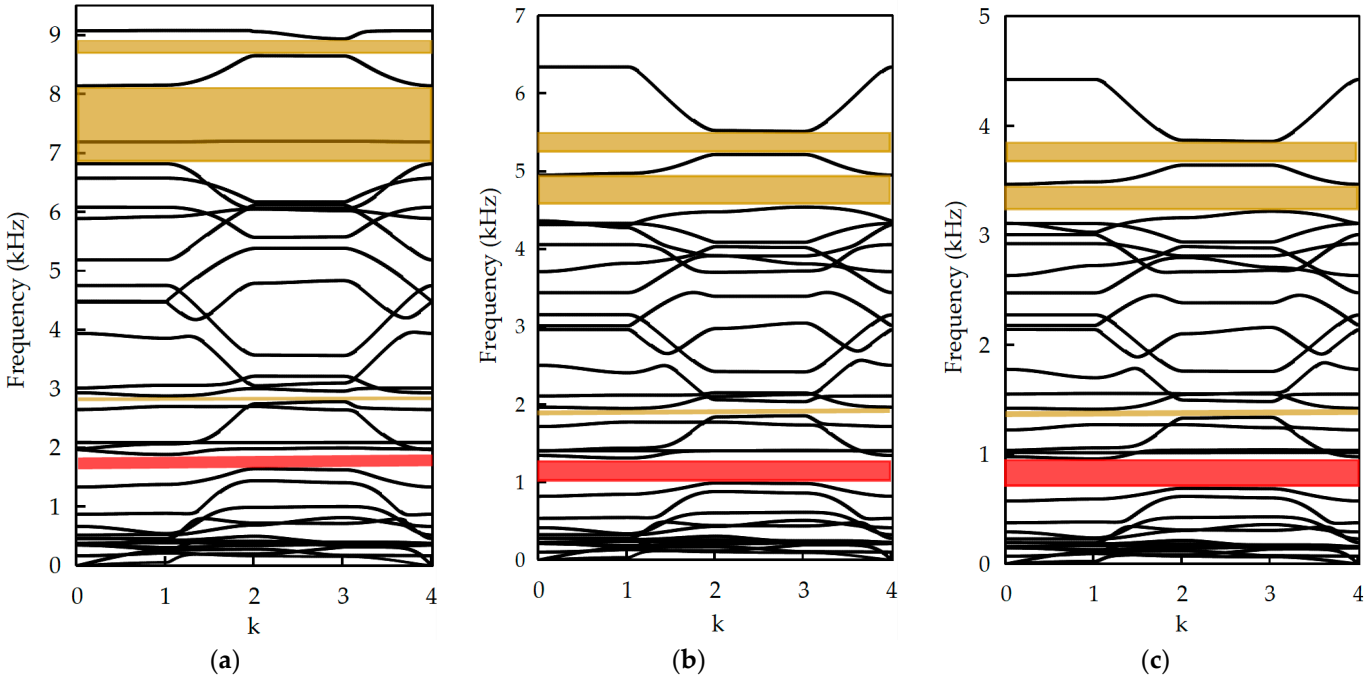


Figure 7. Effect of materials of pins on bandgap of the SPCHM: (**a**) SPCHM with aluminum pins; (**b**) SPCHM with copper pins; (**c**) SPCHM with tungsten pins. The first bandgaps are marked in red and the rest in orange.

4.3.2. Size of the Inserted Pins

According to the previous analysis, altering the size of pins without changing their materials will also have an effect on the vibration modes, and the effect is mainly attributed to two aspects. Firstly, the size of rings should be adjusted to adapt to different sizes of pins, while the overall size of the unit cell remains unchanged, which means that the length of the connecting rods will change together and the frequency of vibration deformation related to the connecting rods will be regulated. Secondly, the relative frequency of vibration deformation between the rods and pins will be adjusted owing to the mass variation of rings. The effect of different sizes of pins on the bandgap distribution is shown in Figure 8, where the pin is made of copper and the radii of the pins are 3 mm, 3.5, mm and 4 mm, respectively. The first bandgaps are indicated in red and the rest in orange.

As shown in Figure 8, the first bandgaps of the three metamaterials occupy the frequency bands from 963 Hz to 1780 Hz, 964 to 1600 Hz, and 988 Hz to 1310 Hz, respectively, and the elastic waves are restrained within these frequency ranges to isolate vibrations. The lower limit of the first bandgap is determined by the mode shape of G2, which is mainly formed by the interaction between the pins and the outside rings; as the deformation of the pins rarely changes regardless of size alteration, the lower limits of the first bandgaps are almost the same. Furthermore, the dispersion curves of the metamaterials move toward low frequencies as the size of pins increases, resulting in a decrease in the upper limit of the first bandgaps.

These results indicate that the bandgaps of the proposed metamaterial are able to be tuned by altering the size of pins. Moreover, this method contributes effective instructions for generating bandgaps in required frequency ranges.

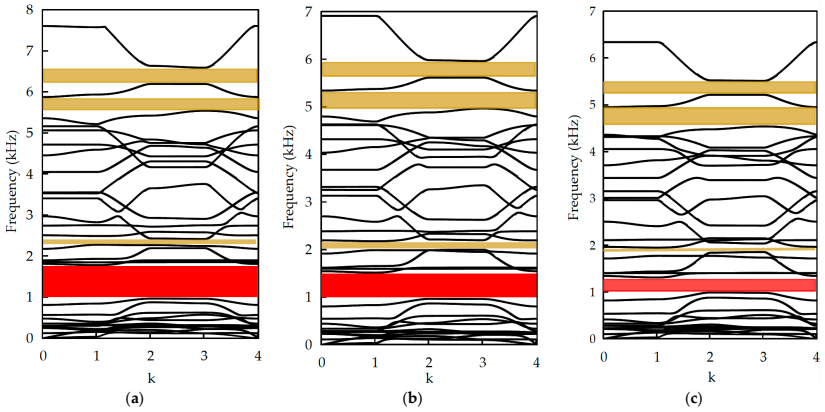


Figure 8. Effect of pin size on bandgap of the SPCHM: (**a**) r_1 = 3 mm; (**b**) r_1 = 3.5 mm; (**c**) r_1 = 4 mm. The first bandgaps are indicated in red and the rest in orange.

4.3.3. Distribution of the Inserted Pins

Each unit cell of the SPCHM contains 14 rings, and this section discusses the influence of different numbers and assembly positions of pins on the bandgap distribution. Figure 9 plots the bandgap distributions of the three SPCHMs with different numbers and assembly positions of copper pins; there are two, five, and seven rings without pins installed, respectively. The first bandgaps are marked in red and the rest in orange.

Compared to Figures 7 and 8, more bandgaps have been generated in Figure 9, especially in Figure 9c, where 11 bandgaps have been generated. This indicates that the number of installed pins has a great impact on opening bandgaps. However, with the increase in bandgaps from Figure 9a to Figure 9c, the bandwidth of the first bandgap becomes narrow and a contradiction exists between the width of the first bandgap and the quantity of bandgaps. In addition, all the dispersion curves are in the low-frequency region below 6000 Hz, making the proposed metamaterial suitable for wide engineering applications.

This method can generate multiple combinations based on different numbers and installation positions of pins, and more bandgap properties will be discovered, which provides a design idea for forming various bandgaps and offers guidance and support for research of low-frequency wide-bandgap metamaterials. Furthermore, if installing different materials of pins in the chosen rings, a better bandgap characteristic may be found.

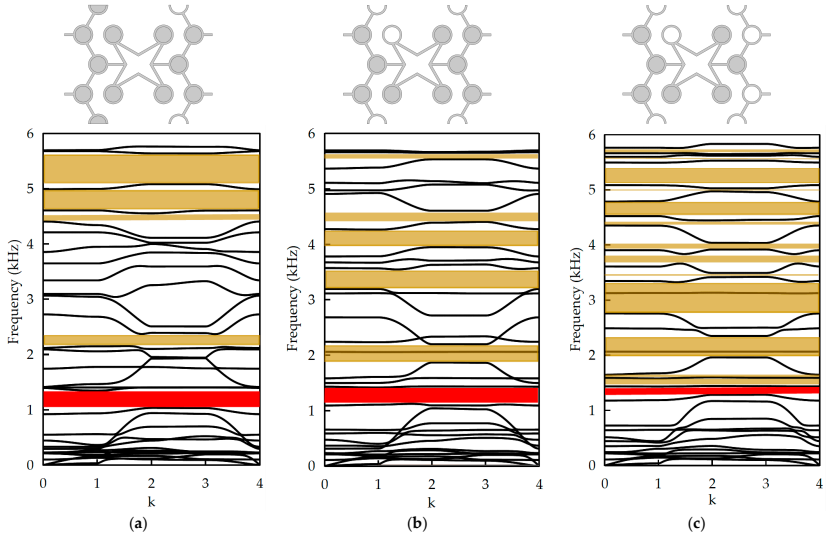


Figure 9. Bandgap properties of the SPCHM with different number and position of pins: (**a**) two rings without pins; (**b**) five rings without pins; (**c**) seven rings without pins. The first bandgaps are marked in red and the rest in orange.

5. Evaluation of Vibration Suppression Performance by Simulation and Experiment

In this section, several simulations and experiments are conducted to verify the vibration suppression performance of the proposed metamaterials. The vibration suppression performance is assessed through the vibration transmission loss (VTL), which is calculated by:

$$\mathrm{VTL} = 20 \times \log_{10}\left(\frac{a_1}{a_2}\right) \tag{7}$$

in which a_1 and a_2 represent the measured values of the output and input acceleration sensors, respectively, and the installation positions of the sensors are shown in Figure 10. It can be concluded from Equation (7) that the proposed metamaterial suppresses vibrations if the VTL value is negative.

The finite element analysis software Abaqus CAE 2018 was used to calculate the VTLs of the metamaterials. In the simulation, the upper and lower aluminum blocks are set as rigid bodies, the output result is the acceleration of the upper aluminum block, and the simulation frequency range is from 1 Hz to 5000 Hz. To ensure the accuracy of the calculation, while ensuring that there are at least 10 elements in the shortest wavelength, the maximum mesh size of the SPCHM is 0.3 mm. Figure 11 reveals that the frequency histories of the VTLs generated from the IM, SPCHM, SPCHM with copper pins, and SPCHM with tungsten pins. All the four metamaterials could effectively restrain vibrations but exhibit different performances. Through Figure 11b–d, the vibration suppression ability of the SPCHM is well enhanced after adding pins into the rings, especially in the low frequency range (within 1000 Hz). As illustrated in Figure 11c,d, the maximum VTL of the SPCHM with copper pins is close to −120 dB, while that of the SPCHM with tungsten pins is about −160 dB; these results indicate that the vibration suppression ability of the SPCHM is able to be regulated by changing the mass distribution inside the rings, which is in accordance with the bandgap characteristic analyzed above. The green marked areas in Figure 11 represent the frequency ranges of bandgaps; the vibration isolation performance of metamaterials is improved within the bandgaps, which implies that the VTL simulation results are in good agreement with the bandgaps.

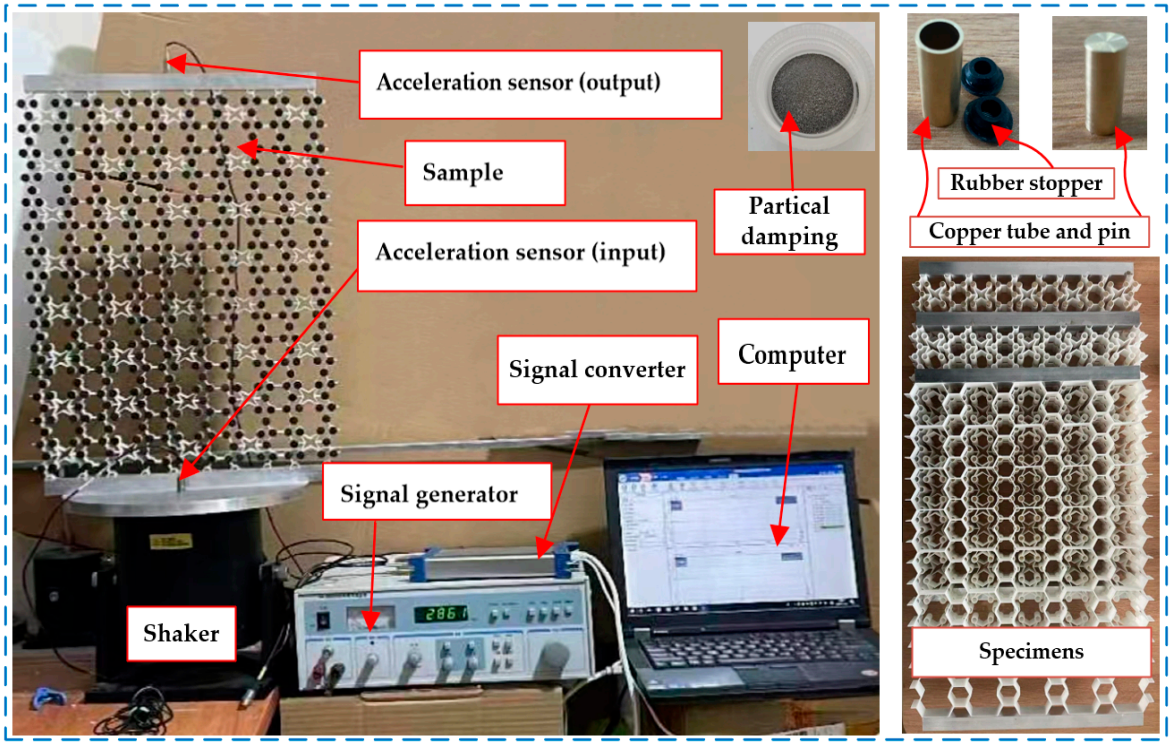


Figure 10. The experimental system.

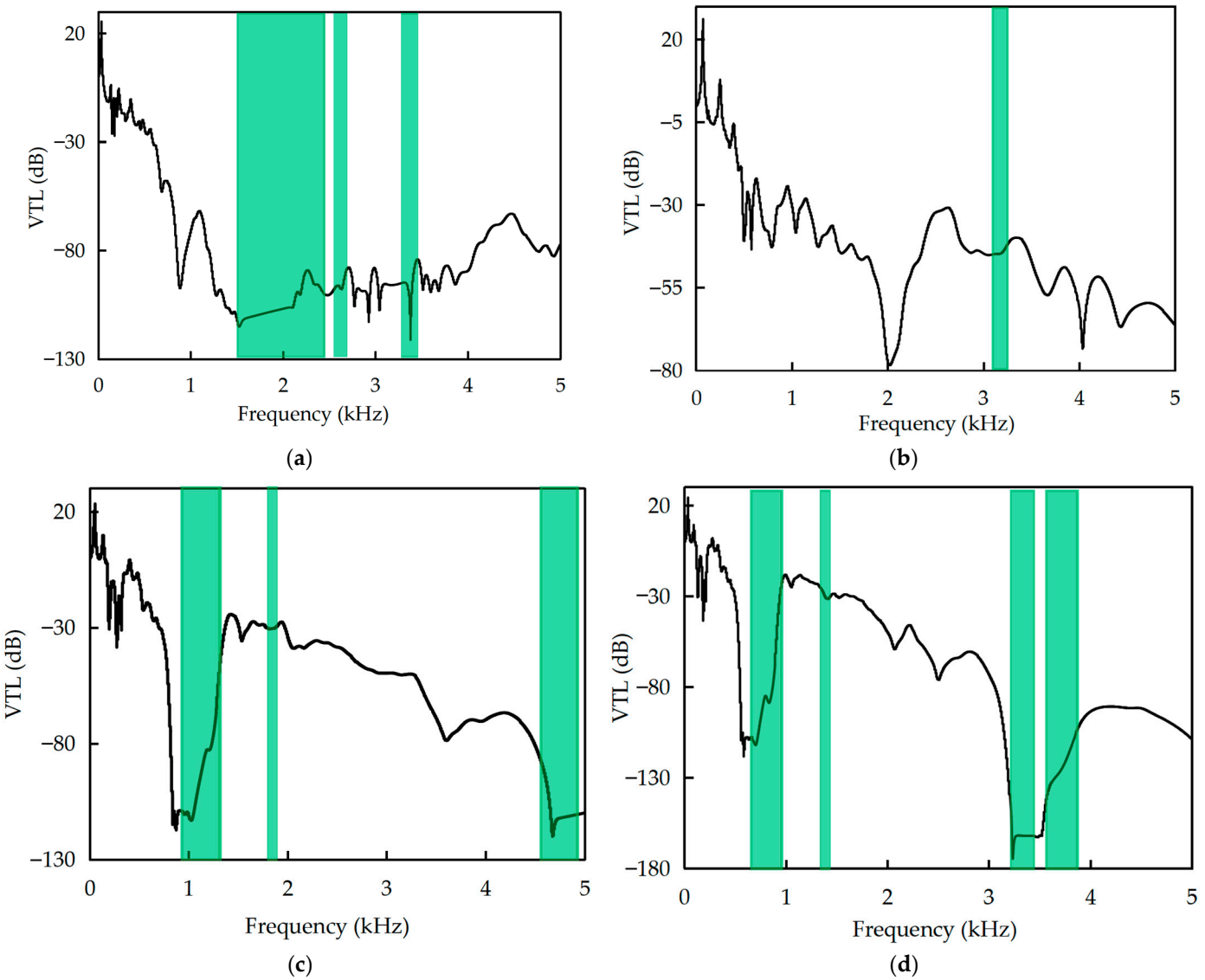
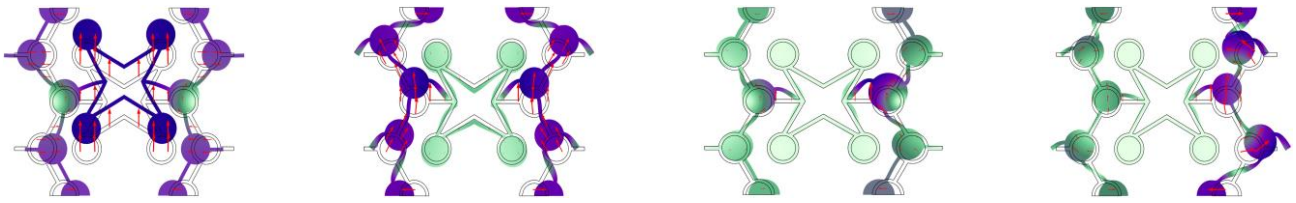


Figure 11. VTL simulation results: (**a**) IM; (**b**) SPCHM; (**c**) SPCHM with copper pins; (**d**) SPCHM with tungsten pins. The green marked areas in Figure 11 represents the frequency ranges of bandgaps.

With the increase in frequency, the vibration modes of the SPCHM show certain characteristics, as shown in Figure 12. The selected k value is 2.5 and the frequencies of Figure 12a–d are 94 Hz, 986 Hz, 3390 Hz, and 5214 Hz, respectively. It can be demonstrated from the figure that, when the frequency is low, the deformation of the unit cell of the SPCHM is manifested as moving and, as the frequency increases, the unit cell is gradually manifested as rotating. When the frequency is large enough, the local deformation behaviors occur on both the left and right sides of the unit cell.



(**a**) k = 2.5, f = 94 Hz (**b**) k = 2.5, f = 986 Hz (**c**) k = 2.5, f = 3390 Hz (**d**) k = 2.5, f = 5214 Hz

Figure 12. The deformation varies with frequency.

As can be seen from Figure 12, the rings move evidently in the low frequency range. In order to further strengthen the suppression ability of vibration excitation outside the bandgap frequency and realize continuous adjustment of the bandgap, metal pipes with particle damping were added inside the rings to replace the metal pins and experiments were carried out to verify its effects.

Figure 10 illustrates the composition of the experimental system. A sweep signal generator is adopted to produce white noise as a system excitation signal, and the frequency automatically sweeps from 2 Hz to 5000 Hz. An electrodynamic vibration shaker is used to realize the excitation signal from the generator. Two acceleration sensors with sensitivities of 1.075 mv/(m·s^{-2}) and 1.067 mv/(m·s^{-2}) are used to sample the input and output acceleration signals at a rate of 10 kHz. The sampling time is 30 s and the signals are converted and transmitted to the computer through a signal converter. The particle damping is made of tungsten powder with a diameter less than 0.25 mm and has been put into the copper tube, followed by plugging both ends of the tube with rubber stoppers. Different samples are installed in the system for testing.

Experimental results of the IM, SPCHM, SPCHM with copper pins, and SPCHM with particle damping are drawn in Figure 13, together with the bandgap regions marked in green. Figure 13a–c point out that the experimental VTLs decrease obviously within the simulated bandgaps, which shows better vibration suppression effect and indicates that the simulation method and results are reliable. Figure 13d displays the comparison of experimental results between the SPCHM with copper pins and the SPCHM with particle damping. The VTL curve of the SPCHM with particle damping locates below that of the SPCHM with copper pins in the whole frequency range, which reveals that adding damping can well enhance the vibration suppression ability of the SPCHM. Noting that the weight of particles is continuously adjustable under the same volume, it has the advantage of replacing any material by designing an equal equivalent density. Moreover, this feature makes it possible to adjust the bandgaps continuously, and the good adaptability of particles provides the potential to be applied in vehicles, transportation devices, aerospace facilities, and other engineering applications with high precision requirements.

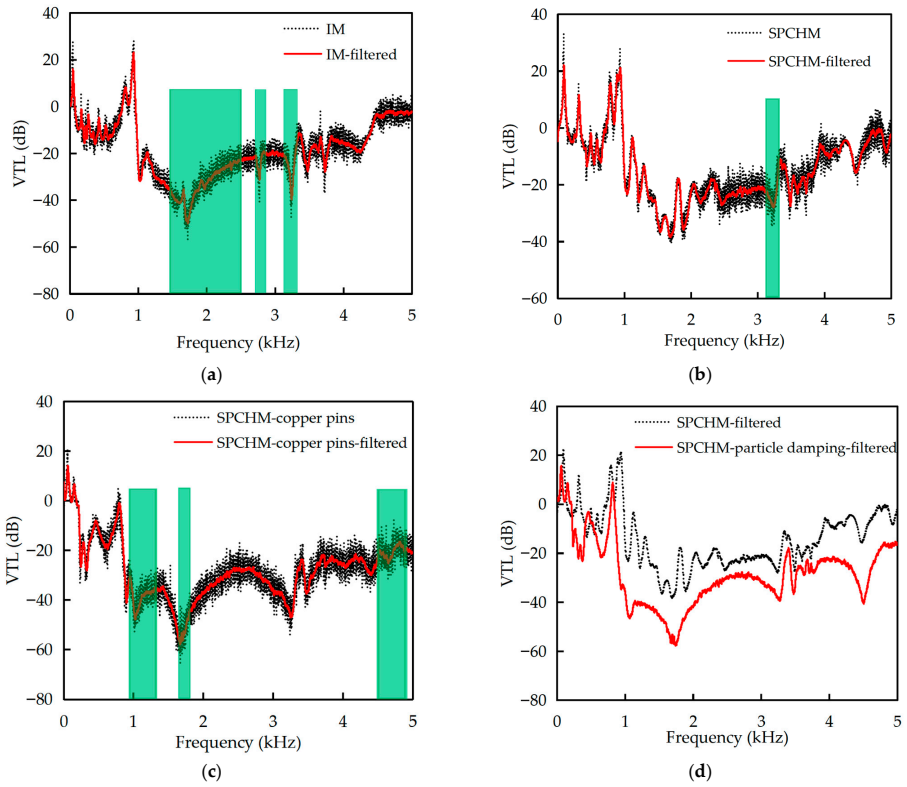


Figure 13. Experimental VTL results: (**a**) IM; (**b**) SPCHM; (**c**) SPCHM with copper pins; (**d**) SPCHM with copper pins; and SPCHM with particle damping.

In general, the metamaterial proposed in this paper has good stiffness and vibration suppression ability, so it has good application potential in the optimization of vehicle suspension system, body, seat, vibration isolation system, ship hull structure, transmission system, propeller, rudder system, and cargo loading device.

6. Conclusions

A novel metamaterial is designed to solve the problem of incompatibility between carrying capacity and vibration suppression performance of common metamaterial. The carrying capacity and vibration suppression capability of the proposed metamaterial are analyzed and verified by simulation and experimental methods. The results show that the carrying capacity of the proposed metamaterial is enhanced by adding rings and assembly pins, and a better vibration suppression capacity is further achieved by adjusting the configuration parameters to generate specific bandgaps. The following conclusions can be drawn from this work:

(1) With the design of rings, the stiffness of the SPCHM has increased by 325% compared to that of the IM, while the mass of the SPCHM is only 23.8% heavier than that of the IM. Moreover, the stiffness of the SPCHM with copper pins has further increased by 62% on the basis of the SPCHM, and the mass of the SPCHM with copper pins is 335% heavier than that of the SPCHM. These features indicate a notable improvement in load-bearing capacity.

(2) The bandgap properties could be effectively regulated by inserting different sizes and materials of pins, thereby improving the vibration suppression performance. Furthermore, more bandgaps will be generated by changing the number and position of pins.

(3) The particle damping method has the advantage of replacing existing materials by designing an equal equivalent density, and it could even be used as a substitute for specific materials that exist in reality. Moreover, this feature makes it possible to adjust the bandgaps continuously, and the good adaptability of particles provides the potential to be applied in engineering applications with high precision requirements.

For a moving automobile, the vibration frequency range of the vehicle body, which is caused by the engine/motor, tires, and wind noise, is generally from 50 Hz to 3500 Hz [45–48]. To improve the environmental perception accuracy for safety and comfort control of intelligent vehicles, our future work will concentrate on the development of a vibration suppression bracket for environmental sensor installation based on the proposed metamaterial. Moreover, adding mixed particle damping of different materials to the rings may produce better results, which will also be the direction for further research.

Author Contributions: Conceptualization, J.Y. and X.H.; methodology, J.Y. and X.H.; software, W.L. and Z.W.; validation, W.L., Y.D. and Z.W.; formal analysis, J.Y. and N.F.; investigation, Y.D. and N.F.; resources, Z.W.; data curation, W.L.; writing—original draft preparation, J.Y. and W.L.; writing—review and editing, J.Y. and X.H.; visualization, Y.D.; supervision, J.Y.; project administration, J.Y. and N.F.; funding acquisition, J.Y. All authors have read and agreed to the published version of the manuscript.

Funding: This research was funded by National Natural Science Foundation of China (No. 52002009), Beijing Natural Science Foundation (No. 3222003), and the State Key Laboratory of Automotive Safety and Energy under Project No. KF2010.

Institutional Review Board Statement: Not applicable.

Informed Consent Statement: Not applicable.

Data Availability Statement: The data that support the findings of this study are available from the corresponding author upon reasonable request.

Conflicts of Interest: The authors declare no conflicts of interest.

References

1. Li, K.; Zhang, Y.; Hou, Y.; Su, L.; Zeng, G.; Xu, X. Mechanical properties of re-entrant anti-chiral auxetic metamaterial under the in-plane compression. *Thin-Walled Struct.* **2023**, *184*, 110465. [CrossRef]
2. Zhu, Y.; Jiang, S.; Zhang, Q.; Li, J.; Yu, C.; Zhang, C. A novel monoclinic auxetic metamaterial with tunable mechanical properties. *Int. J. Mech. Sci.* **2022**, *236*, 107750. [CrossRef]
3. Tan, X.; Chen, S.; Wang, B.; Tang, J.; Wang, L.; Zhu, S.; Yao, K.; Xu, P. Real-time tunable negative stiffness mechanical metamaterial. *Extreme Mech. Lett.* **2020**, *41*, 100990. [CrossRef]
4. Yang, H.; Ma, L. 1D to 3D multi-stable architected materials with zero Poisson's ratio and controllable thermal expansion. *Mater. Des.* **2020**, *188*, 108430. [CrossRef]
5. Tian, Z.; Shen, C.; Li, J.; Reit, E. Programmable Acoustic Metasurfaces. *Adv. Funct. Mater.* **2019**, *29*, 1808489. [CrossRef] [PubMed]
6. Xie, Y.; Fu, Y.; Jia, Z.; Li, J.; Shen, C.; Xu, Y. Acoustic imaging with metamaterial luneburg lenses. *Sci. Rep.* **2018**, *8*, 16188. [CrossRef]
7. Zhang, Z.; Wang, J.; Li, Z.; Zhang, X. Broadband Sound Insulation and Dual Equivalent Negative Properties of Acoustic Metamaterial with Distributed Piezoelectric Resonators. *Materials* **2022**, *15*, 4907. [CrossRef] [PubMed]
8. Rupin, M.; Lerosey, G.; de Rosny, J.; Lemoult, F. Mimicking the cochlea with an active acoustic metamaterial. *New J. Phys.* **2019**, *21*, 093012. [CrossRef]
9. Li, X.; Zhang, H.; Tian, H.; Huang, Y.; Wang, L. Frequency-tunable sound insulation via a reconfigurable and ventilated acoustic metamaterial. *J. Phys. D* **2022**, *55*, 495108. [CrossRef]
10. Lv, J.; Zhou, M.; Gu, Q.; Jiang, X.; Ying, Y.; Si, G. Metamaterial Lensing Devices. *Molecules* **2019**, *24*, 2460. [CrossRef]
11. Jafar-Zanjani, S.; Inampudi, S.; Mosallaei, H. Adaptive genetic algorithm for optical metasurfaces design. *Sci. Rep.* **2018**, *8*, 11040. [CrossRef]
12. Pitchappa, P.; Kumar, A.; Prakash, S.; Jani, H.; Venkatesan, T.; Singh, R. Chalcogenide phase change material for active terahertz photonics. *Adv. Mater.* **2019**, *31*, 1808157. [CrossRef]
13. Thabet, R.; Barkat, O. Transmission Spectra in One-dimensional Defective Photonic Crystal Integrating Metamaterial and Superconductor. *J. Supercond. Nov. Magn.* **2022**, *35*, 1473–1482. [CrossRef]
14. Donnelly, E.; Durant, A.; Lacoste, C.; La Spada, L. Metamaterials for electromagnetic and thermal waves. In Proceedings of the 14th European Conference on Antennas and Propagation (EuCAP), Copenhagen, Denmark, 15–20 March 2020.
15. Balbastre, J.; Nuño, L. Modelling the propagation of electromagnetic waves across complex metamaterials in closed structures. *J. Comput. Appl. Math.* **2019**, *352*, 40–49. [CrossRef]
16. Cong, L.; Savinov, V.; Srivastava, Y.; Han, S.; Singh, R. A metamaterial analog of the Ising model. *Adv. Mater.* **2018**, *30*, 1804210. [CrossRef]
17. Pak, M.; Kim, K.; Pak, H.; Hong, K. Influence of Geometric Structure, Convection, and Eddy on Sound Propagation in Acoustic Metamaterials with Turbulent Flow. *Arch. Acoust.* **2021**, *46*, 637–647.
18. Zhang, Q. Unidirectional electromagnetic wave transmission in hyperbolic-gyroelectric metamaterials. In Proceedings of the Twelfth International Conference on Information Optics and Photonics, Xi'an, China, 1 November 2021.
19. Liao, Y.; Huang, H.; Chang, G.; Luo, D.; Xu, C.; Wu, Y.; Tang, J. Research on Low-Frequency Noise Control of Automobiles Based on Acoustic Metamaterial. *Materials* **2022**, *15*, 3261. [CrossRef] [PubMed]
20. Jung, J.; Kim, H.; Goo, S.; Chang, K.; Wang, S. Realisation of a locally resonant metamaterial on the automobile panel structure to reduce noise radiation. *Mech. Syst. Signal Process.* **2019**, *122*, 206–231. [CrossRef]
21. Li, Y.; Huang, Z.; Xu, Y.; Zhang, H.; Wang, Q.; Qian, H.; Shang, W.; Deng, T.; Cui, K. Scalable-Manufactured Plasmonic Metamaterial with Omnidirectional Absorption Bandwidth across Visible to Far-Infrared. *Adv. Funct. Mater.* **2022**, *32*, 2207239. [CrossRef]
22. Kumar, R.; Kumar, M.; Chohan, J.; Kumar, S. Overview on metamaterial: History, types and applications. *Mater. Today Proc.* **2022**, *56*, 3016–3024. [CrossRef]
23. Zhang, X.; Li, Y.; Wang, Y.; Luo, Y. Ultra-wide low-frequency bandgap design of acoustic metamaterial via multi-material topology optimization. *Compos. Struct.* **2023**, *306*, 116584. [CrossRef]
24. Liu, Y.; Yang, J.; Yi, X.; Guo, W.; Feng, Q. Dimitrios Chronopoulos, Enhanced vibration suppression using diatomic acoustic metamaterial with negative stiffness mechanism. *Eng. Struct.* **2022**, *271*, 114939. [CrossRef]
25. Wang, X.; Wang, L.; Shu, H. Research on dual-functional properties of an improved piezoelectric metamaterial beam for simultaneous vibration suppression and energy harvesting. *Appl. Phys.* **2022**, *128*, 906. [CrossRef]
26. Ye, M.; Gao, L.; Wang, F.; Li, H. A Novel Design Method for Energy Absorption Property of Chiral Mechanical Metamaterials. *Materials* **2021**, *14*, 5386. [CrossRef]
27. Chen, S.; Tan, X.; Hu, J.; Wang, B.; Wang, L.; Zou, Y.; Wu, L. Continuous carbon fiber reinforced composite negative stiffness mechanical metamaterial for recoverable energy absorption. *Compos. Struct.* **2022**, *288*, 115411. [CrossRef]
28. Alomarah, A.; Yuan, Y.; Ruan, D. A bio-inspired auxetic metamaterial with two plateau regimes: Compressive properties and energy absorption. *Thin-Walled Struct.* **2023**, *192*, 111175. [CrossRef]
29. Zhang, Y.; Wang, Y.; Chen, C. Ordered deformation localization in cellular mechanical metamaterials. *J. Mech. Phys. Solids* **2019**, *123*, 28–40. [CrossRef]

30. Dong, P.; Hou, R.; Hu, J.; Lin, C.; Liu, Y.; Qin, L. Novel self-similar re-entrant auxetic metamaterials (SREAM): Design, mechanical property, and geometric optimization. *Polym. Test.* **2023**, *122*, 108015. [CrossRef]
31. Zhang, L.; Pan, F.; Ma, Y.; Yang, K.; Guo, S.; Chen, Y. Bistable reconfigurable origami metamaterials with high load-bearing and low state-switching forces. *Extreme Mech. Lett.* **2023**, *63*, 102064. [CrossRef]
32. Zhang, X.; Ren, X.; Zhang, Y.; Xie, Y. A novel auxetic metamaterial with enhanced mechanical properties and tunable auxeticity. *Thin-Walled Struct.* **2022**, *174*, 109162. [CrossRef]
33. He, H.; Li, Y.; Liu, Y.; Shi, D.Y.; Fan, H.L. Vibration suppression and impact mitigation of locally resonant composite metamaterial columns. *Compos. Struct.* **2023**, *307*, 116631. [CrossRef]
34. Kim, H.-G.; Jeon, O.; Wang, S. A Numerical and Experimental Study on an Interconnected Metamaterial for Flexural Vibration Control Based on Modal Strain Energy. *Appl. Sci.* **2021**, *11*, 4530. [CrossRef]
35. Bai, Y.; Li, X.; Zhou, X.; Li, P.; Beer, M. Soil-expended seismic metamaterial with ultralow and wide bandgap. *Mech. Mater.* **2023**, *180*, 104601. [CrossRef]
36. Das, S.; Dwivedi, K.; Geetha Rajasekharan, S.; Daseswara Rao, Y.V. Vibration attenuation and bandgap characteristics in plates with periodic cavities. *J. Vib. Control* **2021**, *27*, 827–838. [CrossRef]
37. Bae, M.; Oh, J. Nonlinear elastic metamaterial for tunable bandgap at quasi-static frequency. *Mech. Syst. Signal Process.* **2022**, *170*, 108832. [CrossRef]
38. Yang, L.; Wang, L. An ultrawide-zero-frequency bandgap metamaterial with negative moment of inertia and stiffness. *New J. Phys.* **2021**, *23*, 043003. [CrossRef]
39. Bera, K.; Banerjee, A. Ultra-wide bandgap in active metamaterial from feedback control. *J. Vib. Control* **2022**, *28*, 3598–3607. [CrossRef]
40. Muhammad, S.; Wang, S.; Li, F.; Zhang, C. Bandgap enhancement of periodic nonuniform metamaterial beams with inertial amplification mechanisms. *J. Vib. Control* **2020**, *26*, 1309–1318. [CrossRef]
41. Gerard, N.; Oudich, M.; Xu, Z.; Yao, D.; Cui, H.; Naify, C.; Ikei, A.; Rohde, C.; Zheng, X.; Jing, X. Three-Dimensional Trampolinelike Behavior in an Ultralight Elastic Metamaterial. *Phys. Rev. Appl.* **2021**, *16*, 024015. [CrossRef]
42. Zhao, P.; Zhang, K.; Qi, L.; Deng, Z. 3D chiral mechanical metamaterial for tailored band gap and manipulation of vibration isolation. *Mech. Syst. Signal Process.* **2022**, *180*, 109430. [CrossRef]
43. De Ponti, J.; Riva, E.; Ardito, R.; Braghin, F.; Corigliano, A. Wide low frequency bandgap in imperfect 3D modular structures based on modes separation. *Mech. Res. Commun.* **2020**, *105*, 103512. [CrossRef]
44. Ma, N.; Han, Q.; Han, S.; Li, C. Hierarchical re-entrant honeycomb metamaterial for energy absorption and vibration insulation. *Int. J. Mech. Sci.* **2023**, *250*, 108307. [CrossRef]
45. Zheng, X.; Luo, X.; Qiu, Y.; Hao, Z. Modeling and NVH Analysis of a Full Engine Dynamic Model with Valve Train System. *Appl. Sci.* **2020**, *10*, 5145. [CrossRef]
46. Ghosh, A.; Chatterjee, S. An overview on various sources of vibration in electric vehicle and their identification techniques. *J. Braz. Soc. Mech. Sci. Eng.* **2023**, *45*, 401. [CrossRef]
47. Liu, Z.; Yuan, S.; Xiao, S.; Du, S.; Zhang, Y.; Lu, C. Full Vehicle Vibration and Noise Analysis Based on Substructure Power Flow. *Shock. Vib.* **2017**, *2017*, 8725346. [CrossRef]
48. Pizzo, L.; Bianco, F.; Moro, A.; Schiaffino, G.; Licitra, G. Relationship between tyre cavity noise and road surface characteristics on low-noise pavements. *Transp. Res. Part D Transp. Environ.* **2021**, *98*, 102971. [CrossRef]

Disclaimer/Publisher's Note: The statements, opinions and data contained in all publications are solely those of the individual author(s) and contributor(s) and not of MDPI and/or the editor(s). MDPI and/or the editor(s) disclaim responsibility for any injury to people or property resulting from any ideas, methods, instructions or products referred to in the content.